Shear-induced mixing and transport from a rectangular cavity

By E. J. STRANG and H. J. S. FERNANDO

Environmental Fluid Dynamics Program, Department of Mechanical and Aerospace
Engineering, Arizona State University, Tempe, AZ 85287-9809, USA

Measurements were conducted in the vicinity and downstream of two-dimensional cavities filled with a dense miscible fluid subjected to purging by an overlying wall-bounded turbulent shear flow. Two cavities with aspect ratios 1 and 2 were used, based on previous observations that the mechanism for entraining dense fluid into the flow above is different for these cases. Scaling for the downstream variation of the vertical concentration (buoyancy) distribution of dense fluid is advanced based on dimensional arguments and tested using laser-induced fluorescence measurements. The mean flow and turbulent statistics in the vicinity and downstream of the cavity were also measured. A notable increase of shear stress and turbulent intensities was observed above the higher aspect ratio cavity due to intense vertical exchange between the cavity and the flow above. The influence of the cavity could be detected for several cavity widths, or distances equal to several eddy turnover times. However, the flow above the lower aspect ratio cavity exhibits dramatically less vertical exchange between the cavity and the flow above, as indicated by subtle wisps of fluid transported downstream by the free-stream flow. The shear stress and turbulent intensities for this case have only a minor influence of the cavity.

1. Introduction

The removal of contaminants trapped in natural or man-made canyons by an overlying mean flow is of interest in environmental fluid mechanics. For example, in rivers and lakes, dense water accumulates in bottom depressions, creating stagnant pools that can be harmful to the surrounding ecosystem. Lack of flushing (or purging) and circulation in such pools leads to hypoxic conditions, making them uninhabitable for fish and other aerobic organisms (Debler & Armfield 1997). Another example is the carbon sequestration to mitigate environmental impacts of CO_2 emissions from power plants. One proposed remedy is to dump compressed liquefied CO_2 into the ocean bottom. It has been of long-standing interest to understand how such liquid CO_2 is flushed out of benthic ponds, mixed with saline water and dispersed downstream along the ocean bottom, so that the environmental impacts of the process can be assessed.

In another vein, a significant fraction of the world's population is concentrated in areas of complex terrain characterized by basin-shaped topography, and the degree to which dense air is pooled in such basins at night and then purged by overlying synoptic flow has severe implications on the air quality within. Without adequate flushing, toxic air pollutants accumulate in the basin, causing health hazards. Also, with the spectre of biological and chemical warfare in sight, it has become necessary

to understand how a release of airborne material into an urban canyon or to an entire urban basin is dispersed and diluted downstream by an existing mean flow so that estimates can be made of the safe tactical perimeter for emergency evacuations.

The above scenarios are just a few examples of the many instances where we observe the transport of material from a cavity into an overlying flow and are concerned with its dispersion and mixing downstream of the cavity. Owing to substantial practical applications of the problem, several studies have been performed on the removal of either neutrally buoyant or negatively buoyant fluid from topographic depressions by an overlying mean flow. Most of these studies have been performed with two-dimensional rectangular, V-shaped or trapezoidal cavities (with bottom and brim length scales of L_1 and L_2, respectively, and depth H) filled with a 'contaminated' (dyed) fluid up to a depth h. Steady-state experiments wherein h is maintained by injecting dense fluid to make up for purging (Briggs, Thompson & Snyder 1990), experiments with no pooling within the cavity and immediate purging of contaminants introduced into the cavity (Castro *et al.* 1993) and unsteady experiments with flow over a dense pool with varying h (e.g. Seeto 1987; Debler & Imberger 1996; Debler & Armfield 1997) have been conducted. The purging process appears to be dependent on the internal Froude number $Fr = U_o/\sqrt{\Delta b_o H}$ and of course on the cavity geometry. Here U_o is the approaching free-stream velocity and Δb_o is the buoyancy jump between the cavity and background fluids.

For trapezoidal and rectangular cavities, purging occurs rapidly ('one-shot' mode) for $Fr > 1.5$–2.0 whereas at lower Fr the buoyancy forces retard the removal (Debler & Imberger 1996). For $Fr \ll 1$, the purging depends on the rate at which turbulent entrainment occurs across the interface that separates the dense and overlying fluid layers. Several entrainment mechanisms are possible therein, including splashing of dense fluid into the stream, seiching at the interface, scooping of the lower fluid by the overlying flow and internal wave breaking (Fernando 1991). For V-shaped cavities with $Fr \ll 1$ and high Reynolds numbers, the volume flux removal rate (per unit streamwise length) appears to be $v_o \sim U_o^3/\Delta b_o$, for both steady and unsteady flows (Briggs *et al.* 1990). Empirical parameterizations for removal rates that account for geometrical differences have also been proposed, based on experiments carried out with a range of aspect ratios $A = L_2/H$ (Armfield & Debler 1993). These experiments show that a forced vortex is generally formed within short depressions ($A < 1$) with the vertical fluid transport out of the cavity primarily governed by molecular diffusion whereas for longer depressions the transport occurs by entrainment due to interfacial instabilities.

Despite considerable research on the purging problem under various flow and geometric conditions, to our knowledge literature on the downstream distribution of purged material is virtually non-existent. As already stated, such information is imperative in planning emergency response for accidental spills (or deliberate releases) of contaminants. The work described herein deals with the downstream distribution of contaminants upon their removal from a cavity by an overlying flow. For simplicity, a cavity with vertical sidewalls is considered, which is also associated with gravest purging conditions (Castro *et al.* 1993). The experimental configuration consists of a rectangular cavity in a channel, filled with dense fluid, subjected to a turbulent flow above. The mean flow and turbulent fields near the cavity and the distribution of material flushed out of the cavity are studied experimentally.

The paper is organized as follows. The dimensionless governing parameters for the problem are identified in §2. The experimental preparation and procedure is described in §3. Velocity and turbulence measurements in the limit $Ri \rightarrow 0$ are presented in §4
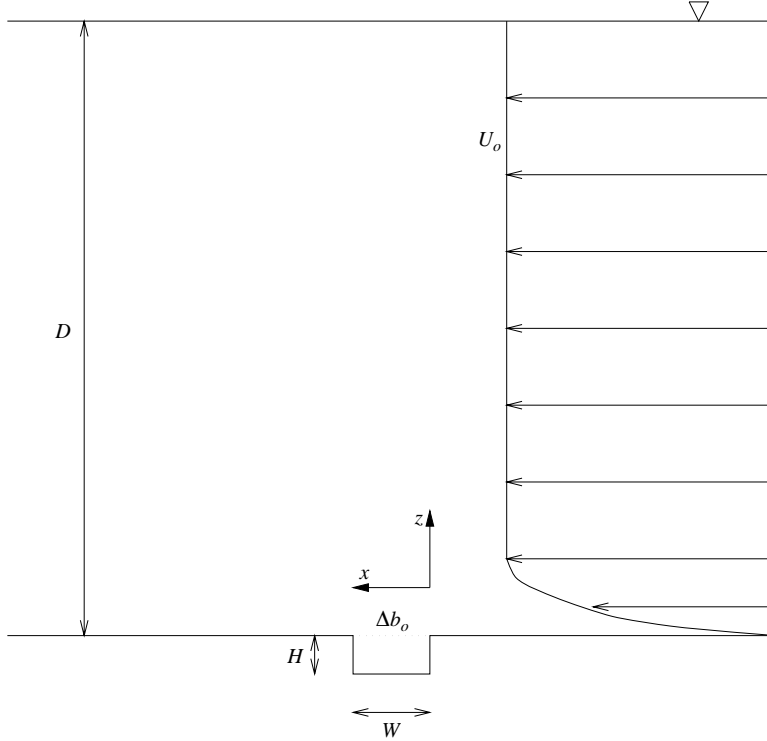
FIGURE 1. A schematic of the channel flow over a transverse, rectangular cavity containing heavy fluid.

as a baseline case that can be used to interpret experiments with dense fluid in the cavity. Measurements of the concentration distribution and appropriate scaling are described in §5. The conclusions of the paper are given in §6.

2. Theoretical preliminaries

A schematic of the flow configuration to be used is shown in figure 1, where purging of heavy fluid from a two-dimensional cavity of dimensions $(W \times H)$ filled with a dense contaminant is considered. The background flow is a turbulent channel flow of depth D with a free-stream velocity U_o. The governing parameters for the problem are U_o, W, H, D, the buoyancy jump across the interface between the cavity and free-stream fluids Δb_o and the molecular parameters κ (molecular diffusivity of the contaminant) and ν (kinematic viscosity of the fluid). Thus, any dependent parameter Π at a given location can be written as

$$\Pi = \Pi(H, W, D, U_o, \Delta b_o, \nu, \kappa). \qquad (2.1)$$

Since our interest is purging when the cavity is full or near-full, the depth of the fluid layer in the cavity is H, and hence not included as a separate parameter. Therefore, any non-dimensional parameter Π^* may take the form

$$\Pi^* = \Pi^*(A, Ri, Re, Pe, H/D), \qquad (2.2)$$

where $A = W/H$ is the cavity aspect ratio, $Ri = \Delta b_o H/U_o^2$ is the bulk Richardson number ($= 1/Fr^2$), $Re = U_o D/\nu$ is the Reynolds number, $Pe = U_o D/\kappa$ is the Péclet

number and H/D is the ratio of the cavity depth to the channel flow depth. Assuming Reynolds and Péclet number similarities that ensure the independence of Π^* from Re and Pe at high Re and Pe, and the fact that $H/D \to 0$, the non-dimensional set in (2.2) can be reduced to

$$\Pi^* = \Pi^*(A, Ri). \tag{2.3}$$

Note that the Reynolds number used here is in an intermediate range from 1.5×10^4 to 4×10^4 (or the related parameter, the Reynolds number based upon the momentum thickness, $2500 < Re_\theta < 4000$). The experimental parameters were selected so that the Reynolds numbers are sufficiently high to ensure the similarity conditions assumed above. The adequacy of Re values used were checked using: (i) the measurement of spectra of longitudinal velocity in the turbulent layer, which, when scaled with integral scales, collapsed to a single curve within error bars, (ii) the presence of a significant inertial subrange in the spectrum, and (iii) the agreement of turbulent boundary layer measurements made without the cavity with similar previous measurements made at higher Re (e.g. agreement of constants in the wall and logarithmic regions).

3. Experimental procedure

Concentration and velocity field measurements were performed proximate to the rectangular cavity underlying the turbulent channel flow boundary layer. The channel flow was established in a closed-loop water channel facility, similar in design to that of Odell & Kovasznay (1971); see figure 2. Through the action of two counter-rotating series of disks (separated in the vertical by 1 cm), horizontal momentum was imparted to the channel flow (for details of the channel construction as well as flow conditioning, see Strang & Fernando 2001). The tests were made in the straight section of the channel, as indicated in figure 2.

Midway through the straight test section (opposite the pump section of the elongated circular facility), a rectangular cavity was inserted within the channel floor, normal to the flow direction, i.e. the cavity runs across the channel floor from wall to wall (channel width approximately 30 cm). Experiments were performed for a cavity depth H of 1.27 cm and cavity widths of 1.27 and 2.54 cm. A total water depth of $D = 35$ cm was used during all experiments.

Prior to initializing the channel flow, the rectangular cavity was slowly filled with dense saline solution to the level of the channel floor. This saline solution was dyed with Fluorescein (concentration ~ 50 p.p.m.). In order to maintain a nearly constant level of dense (dyed) saline solution in the cavity, additional saline solution was injected into the cavity bottom during the experiment using an array of flexible tubing (1.58 mm, or 1/16 in. diameter) fed by a manifold located at the base of a constant-head reservoir. Since the dense fluid in the cavity receded slowly, only a carefully metered amount of make-up fluid needed to be supplied intermittently.

Once the initial filling of the cavity was complete, a plastic cover was slowly positioned over the top of the cavity, and the channel flow was initiated shortly thereafter. When the free-stream velocity reached a steady state (as evidenced by laser-Doppler velocimeter measurements), the plastic cover was slowly removed sideways and up, allowing the cavity to be exposed to the overlying flow. Within approximately 10 s from the removal of the plastic cover, the initial perturbations (generally accompanied by a sudden surge at the fluid interface and release of blobs of fluid which flushed away downstream) rapidly decayed allowing the concentration measurements to be performed in a quasi-steady state. As mentioned above, the
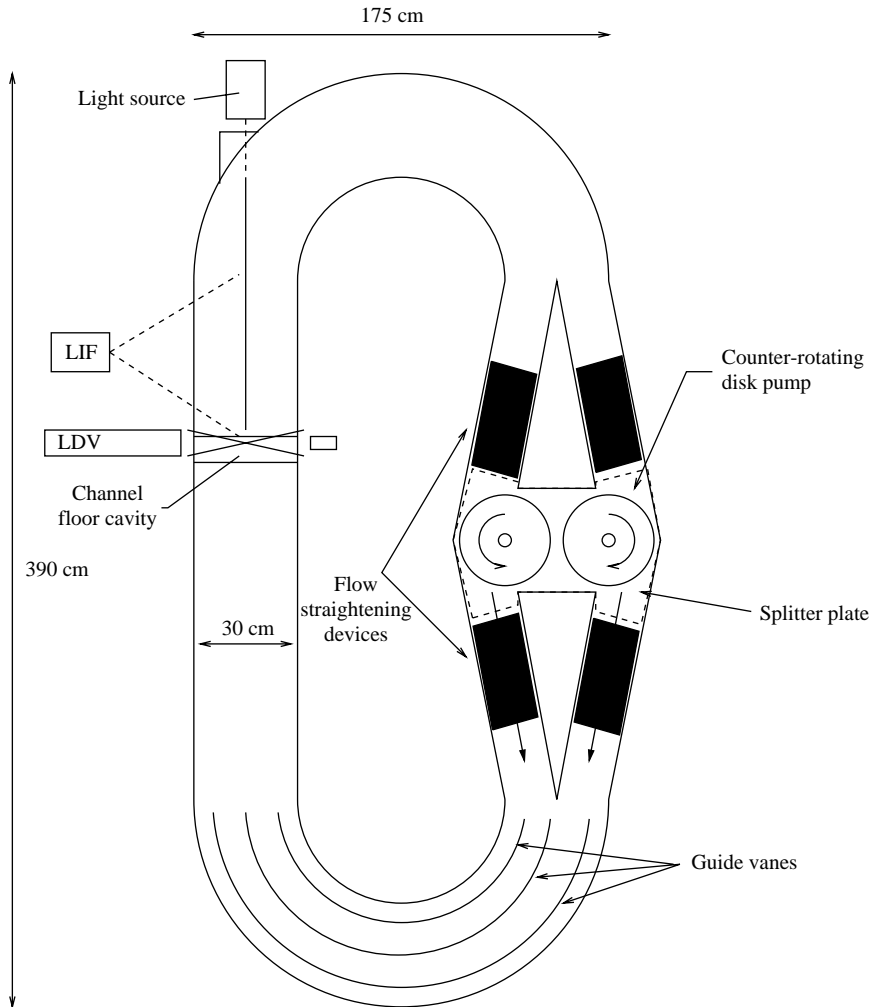
FIGURE 2. The Odell–Kovasznay channel used for experiments. This apparatus is a recirculating water facility capable of producing a channel flow of dimensions 35 cm height and 30 cm width with flow speeds in the range of approximately 2 to 15 cm s^{-1}. The flow is driven by a disk pump the plates of which rotate in counter directions and push the fluid forward as shown. After the pump disturbances have decayed and fluid leaves the curved section, an approximately uniform channel flow can be realized. This occurs within 30 to 60 cm into the straight section. For details of flow management in the channel, see Strang & Fernando (2001). The channel is made of Plexiglas, except the test section which was made of tempered glass.

dense fluid layer in the cavity was maintained constant throughout the experiment by intermittently feeding the cavity with fresh fluid from below. The decrease in the dense fluid layer in the cavity occurred over a time scale significantly larger than the sampling time scale, and hence the slow injection of make-up fluid is expected to have a negligible influence. For example, the sampling time T was typically less than 10% of the time the cavity fluid level h takes to recede by 10% the cavity depth H without the additional injection of the saline solution; namely $T < 0.1[0.1H(\mathrm{d}h/\mathrm{d}t)^{-1}]$. The sampling period T for concentration-field ensemble averaging was generally chosen to be $T = 15\,\mathrm{s}$.

The measurement programme included both the concentration and velocity fields. The latter was conducted first, in the absence of dense fluid in the cavity, to provide flow information for interpreting the concentration data and to ensure that the flow obeys Reynolds number similarity.

A custom-built, single-component laser Doppler velocimetry (LDV) system was used for velocity field measurements. The vertical thickness of the LDV sampling volume was approximately 1 mm and, since in this study a wall unit is approximately 0.5 mm, the closest reliable measurement to the channel floor was approximately 3 to 5 wall units. This limitation is common in all (recirculating) water channel facilities. However, as will be observed later, this measurement is sufficiently close to the channel floor to be within the viscous sublayer and achieve an adequate measure of the friction velocity (the velocity gradient within the viscous sublayer is constant).

Concentration measurements were made using a standard laser-induced fluorescence (LIF) system (e.g. Strang & Fernando 2001). The operation of this system relies on the ability of fluorescein to absorb argon-ion light at approximately 490 nm and emit at approximately 520 nm. The emitted light intensity depends on the dye concentration. Thus by selectively collecting the light at the latter wavelength and using a suitable calibration (for concentrations <50 p.p.b., the light intensity is proportional to the concentration) the dye concentration could be calculated. As is commonly done, in the present experiments, a two-dimensional swath of the flow at the centre of the channel was illuminated by an argon-ion laser beam and the illuminated section was recorded using a video camera onto SVHS tapes after the light passes through a ∼500 nm cut-off lens. Therefore, the intensity of light recorded is directly proportional to the dye concentration. As shown in figure 2, a parallel beam scanner (DeSilva, Montenegro & Fernando 1990) was used to obtain a sheet of argon-ion light of 0.9 mm thickness and 8 cm in height. Details of this technique are further described in Strang & Fernando (2001).

When measuring the concentration boundary layer thickness (see § 5), typically 1000 frames were analysed, taken at a rate of 30 frames per second (60 fields per second). The measurement resolution in the (x, z)-plane was evaluated to be 0.5 mm. In each frame, raw pixel intensities (0–255) were converted to actual dye concentration using *a priori* calibration of the system with solutions of known dye concentration. For example, the channel flow was dyed with a known amount of fluorescein dye to produce a homogeneous solution, and, thereafter, illuminated by the argon-ion laser sheet. The fluorescent light intensity was recorded for progressively greater dye concentrations to establish a relationship between dye concentration and light intensity. The range of dye concentration was selected to ensure a linear relationship between light intensity and dye concentration, as well as to ensure negligible (<5%) attenuation of the laser sheet light intensity due to absorption. By knowing the initial salt and dye concentrations in the cavity solution, the density, salt concentration, and buoyancy (defined as $b = (\rho - \rho_o)g/\rho_o$, where ρ_o is the reference density) variation downstream of the cavity could be calculated by measuring the downstream distribution of dye concentration. In the analysis of data, it is assumed that the dynamics of dye and salinity fluctuations are the same. This follows from the fact that the diffusivities of salt and dye are of the same order and that large-scale fluctuations are evolved and dissipated with a time scale of the order of the integral length scale, independent of molecular diffusivities (Fernando & Hunt 1996).

In general, standard data processing techniques were used for processing of LIF images and LDV measurements (Strang & Fernando 2001). For LIF concentration measurements, the errors in the mean concentration and r.m.s. of concentration fluctuations
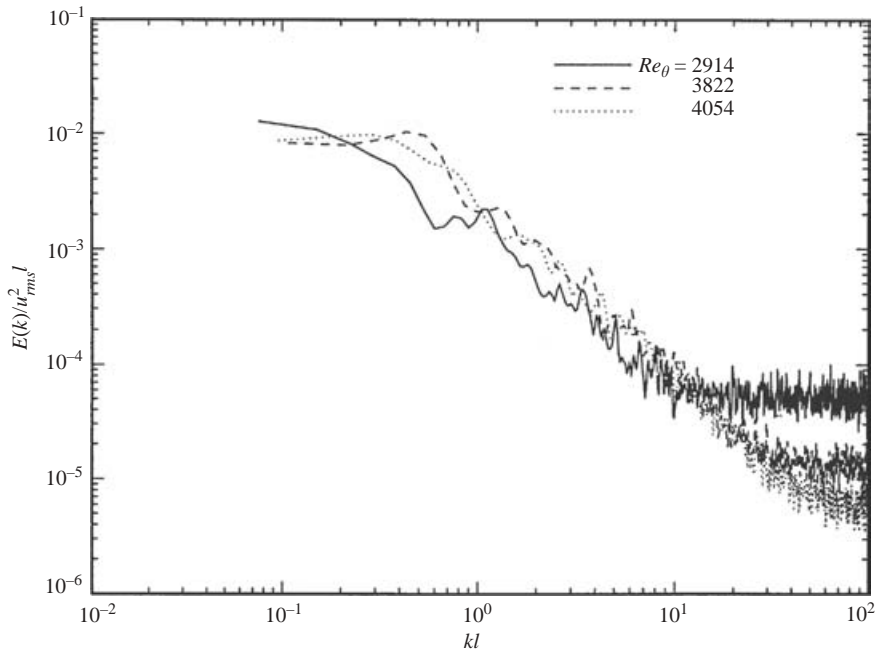
FIGURE 3. The free-stream wavenumber spectrum for the streamwise velocity normalized using an r.m.s. streamwise velocity u_{rms} in the free-stream and the integral length scale l; $Re_\theta = $ 2914, 3822 and 4054.

were $\pm 5\%$ and $\pm 10\%$, respectively. Similarly, for the velocity measurements using LDV, the errors in the measurement of the mean streamwise velocity and the r.m.s. of velocity fluctuations were $\pm 7\%$ and $\pm 10\%$, respectively.

4. Velocity field measurements in the limit $Ri \rightarrow 0$

As a precursor to concentration measurements, velocity measurements were made in the absence of heavy fluid in the cavity ($Ri \rightarrow 0$) to investigate the upstream conditions, the flow adjustment surrounding the cavity, and the degree to which the Reynolds number similarity discussed in §2 is satisfied. In the first series of experiments, the cavity with $A = 2$ was used. The streamwise velocity measurements were made with the single-component LDV (§2) at the centre of the channel at the half water depth. The aim here was to investigate whether the turbulence in the channel is sufficiently strong to justify the use of classical concepts pertinent to turbulent channel flows. The measured longitudinal spectra normalized by the quantities involving the r.m.s. velocity and integral length scale are shown in figure 3 for three different Reynolds numbers. The sampling was done over a time period of 32 s (sufficiently larger than the integral time scale) at a frequency of 256 Hz, and Taylor's hypothesis was employed in calculating the spectra.

Note that, upon normalization by integral-scale quantities, the data in the inertial subrange part of the spectra collapse reasonably well, within the experimental error margin of $\pm 20\%$, indicating support for the Reynolds number similarity. The collapse between the two higher Reynolds numbers ($Re_\theta = 3822$ and 4054) is better, with the lower $Re_\theta = 2914$ lying somewhat below. The Reynolds number ranges used, however, were limited because of experimental limitations. The presence of a $k^{-5/3}$ spectral
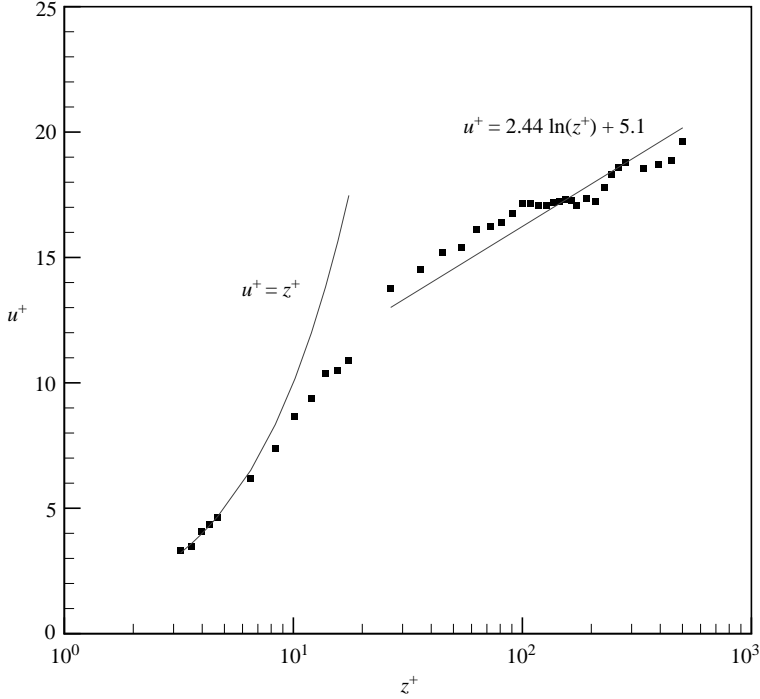
FIGURE 4. Normalized vertical profile of streamwise velocity for a smooth flat channel floor; $Re_\theta = 3822$.

region over a decade for $Re_\theta = 2914$ and over two decades for the higher Reynolds numbers clearly indicates that the Reynolds numbers used are high enough for fully developed turbulence to exist in the channel and for Reynolds number similarity. In the second series of experiments, measurements were conducted $8W$ upstream of the cavity in order to check the nature of approaching velocity profiles. Figure 4 shows the mean velocity u measurements, which indicate that the classical logarithmic law

$$u^+ = \frac{1}{\kappa} \ln z^+ + a, \qquad (4.1)$$

where $u^+ = u/u_*$ and $z^+ = z/(\nu/u_*)$ are wall variables, $\kappa = 0.41$ is the von Kármán constant, and u_* is the surface friction velocity evaluated using

$$u_* = \left(\nu \frac{\partial u}{\partial z} \bigg|_{z=0} \right)^{1/2}, \qquad (4.2)$$

is valid with the canonical value of $a \simeq 5.1$ (Bernard & Wallace 2002). In evaluating u_* using (4.2), the law of the wall $u^+(z^+) = z^+$ was used, and the streamwise velocity data points closest to the wall permitted by the LDV system ($z^+ \sim 5$) were employed. The reproduction of the classical law of the wall and log-layer also indicate the reliability of the measurements.

In the next series of experiments, measurements of the vertical distribution of mean streamwise velocity and r.m.s. velocity were performed at one cavity width ahead of the leading edge, at the leading edge, the trailing edge, and at intervals of one cavity width downstream of the trailing edge up to seven cavity widths. Figure 5(*a*, *b*) presents the vertical profiles of streamwise velocity at various locations for aspect
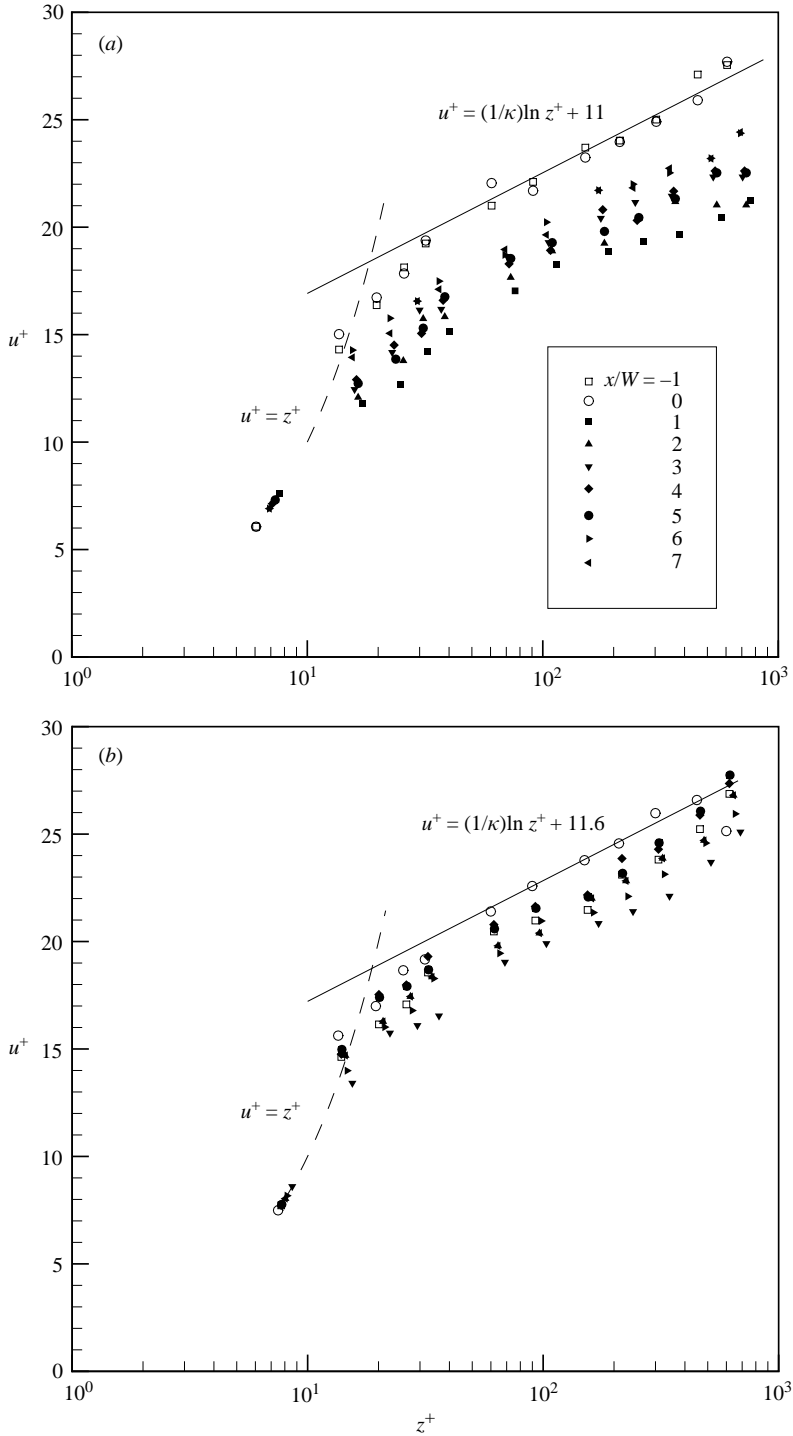
FIGURE 5. Normalized vertical profile of streamwise velocity at multiple streamwise locations: (*a*) Cavity aspect ratio $A = 2$, and (*b*) $A = 1$. $Re_\theta = 3822$.
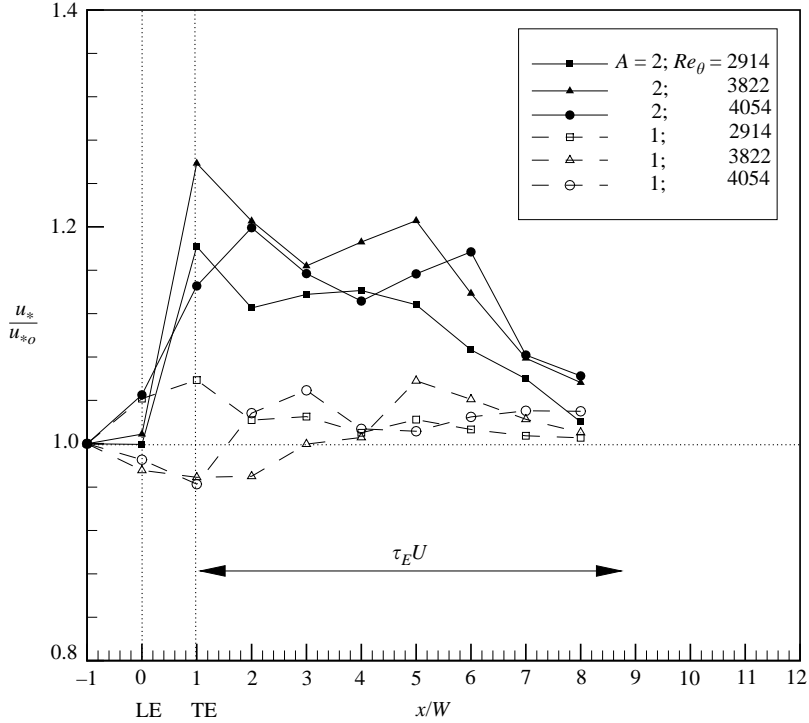
FIGURE 6. The variation of normalized friction velocity downstream of the cavity. LE – leading edge; TE – trailing edge. The displacement of a fluid parcel in the free stream corresponding to an eddy turnover time is shown.

ratios $A = 1$ and 2. The local and the normalized velocities are plotted as a function of wall units $z^+ = zu_*/\nu$. The variation of the local friction velocity was evaluated using the same technique as before, and its spatial variation, with the measurements normalized by the upstream ($x = -W$) value, is shown in figure 6. A marked increase of u_* can be seen over the cavity for $A = 2$, in consonance with the rapid increase of Reynolds stresses therein. Djenidi, Elvarasan & Antonia (1999) have attributed such an increase to the inflow and outflow events surrounding the cavity, which cause substantial exchange of horizontal momentum vertically, leading to enhanced Reynolds stresses. The wider cavity $A = 2$ permits the development of a shear layer and its breakdown, and the Reynolds stresses are higher therein. Also shown in figure 6 is the distance fluid parcels in the free stream travel over a typical turnover time of turbulent eddies, where τ_E was calculated as the ratio of the longitudinal integral length scale to the free-stream velocity U_o. The longitudinal integral length scale was determined from integrating the autocorrelation of streamwise velocity fluctuations.

It appears that the relaxation of turbulence induced by the cavity is taking place on a time scale of the order of an eddy turnover time scale downstream, which is the same time scale over which the turbulent kinetic energy spectrum relaxes in response to perturbations occurring at larger scales. Furthermore, it is evident in figure 6 that the normalized friction velocity downstream of the cavity does not show a substantial dependence on the Reynolds number Re (or Re_θ).

The overall effects of the cavity on downstream and mean flow turbulence can be quantified by hypothesizing that the effects of the cavity can be treated as equivalent

distributed roughness elements of height k; see Nezu & Nakagawa (1993). Then, in the region of influence of the cavity, there are two wall length scales, k and ν/u_*, leading to a log-layer velocity profile of the form (Tennekes & Lumley, p. 164)

$$u^+ = \frac{1}{\kappa} \ln z^+ + g(R_k), \tag{4.3}$$

where $u^+ = u/u_*$ and $z^+ = z/(\nu/u_*)$ are wall variables, κ is the von Kármán constant, as before, and $g(R_k)$ is a roughness function where $R_k = u_* k/\nu$ is a Reynolds number based on the roughness height. Past experiments with distributed roughness show that when $R_k < 5$ the roughness has no effect and (4.3) takes the smooth-wall form (4.1). For $5 < R_k < 70$, the flow feels the effects of both roughness and viscous effects (Nezu & Nakagawa 1993). For $R_k > 70$, equation (4.3) becomes independent of viscous influence with $z^+ \to z/k$ and $g(R_k) = $ constant (Schlichting 1987). Although the overall influence of a single roughness element is not known, it is possible, at least qualitatively, to describe the effect of the cavity using the roughness Reynolds number $R_k = u_* H/\nu$ (where H is 1 cm). The estimated range is 75–278 (k constant and u_* varies), and thus the influence of the cavity is expected to be significant in determining the velocity profiles.

The measurements shown in figures 5(a, b) are consistent with some of the general concepts described above for the distributed roughness. For example, in figure 4 ($Re_\theta = 3822$), far upstream ($x = -8W$) of the cavity the flow obeys the classical scaling (4.1) with $a \simeq 5.1$, but the measurements just upstream of the cavity ($x = -W$) indicate that the profile has been modified, arguably following the logarithmic form with $a \simeq 11$. The same profile remains for $x = 0$ (leading edge of the cavity) and $x = W$ (trailing edge of the cavity), and $g(R_k)$ then reverts to smaller values as the friction velocity slowly relaxes downstream. From the results, it is clear that the flow distortions by the cavity persist at least for distances up to $8W$.

Assuming that the profiles downstream of the cavity follow a logarithmic law, as in (4.3) for distributed roughness, $g(R_k)$ was calculated for the profiles shown in figure 5(a). The values varied in the range $5 < g(R_k) < 11$, in agreement with the range observed in experiments with distributed roughness; it first increases from 6 (at $R_k \sim 2$) to about 9.5 ($R_k \sim 10$) and then decreases to 8.5 for $R_k > 70$ (which is the completely rough regime; Schlichting 1987, p. 620). In particular, for the profiles taken downstream of the cavity ($x > 0$), $g(R_k)$ is in the range of $6 < g(R_k) < 9$, indicating the possibility of representing a single roughness element in terms of an 'equivalent' distributed roughness.

The observations for $Re_\theta = 3822$ with $A = 1$ are generally similar, but the details vary. On either edge of the cavity, $g(R_k)$ is higher, and downstream $g(R_k)$ varies between 6 and 10. In this case also the flow did not relax back to the far upstream profile over the downstream measurement distance $8W$.

Figure 7(a, b) presents the normalized (by local u_*) r.m.s. velocity distributions for cases shown in figure 5(a, b). The general collapse of data within error bars indicates the suitability of u_* for scaling the turbulent velocities. For $A = 2$, this represents a clear increase of local (dimensional) turbulent kinetic energy downstream. This increase is lesser for $A = 1$ (cf. figure 6). The solid line in figure 7(a) represents the theoretical distribution of the r.m.s. velocity in the near-wall boundary layer ($z^+ < 100$) given by

$$\frac{u_{rms}}{u^*} = D_u \mathrm{e}^{-z^+/R^*} \Gamma(z^+) + C z^+ (1 - \Gamma(z^+)), \tag{4.4}$$
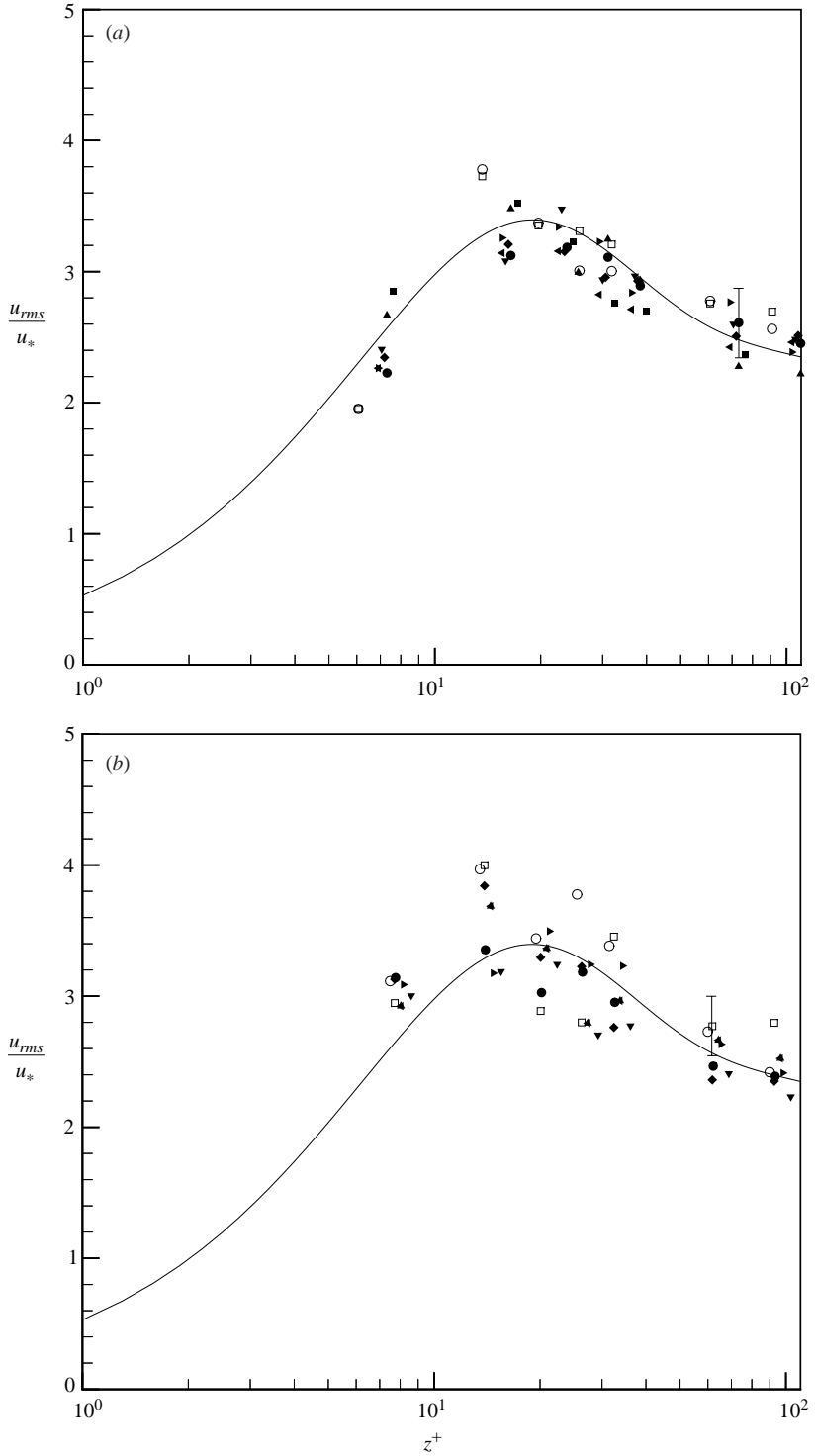
FIGURE 7. Normalized vertical profile of r.m.s. streamwise velocity at multiple streamwise locations: (*a*) Cavity aspect ratio $A = 2$, and (*b*) $A = 1$. $Re_\theta = 3822$. The solid line indicates (4.4). Symbols as figure 5.
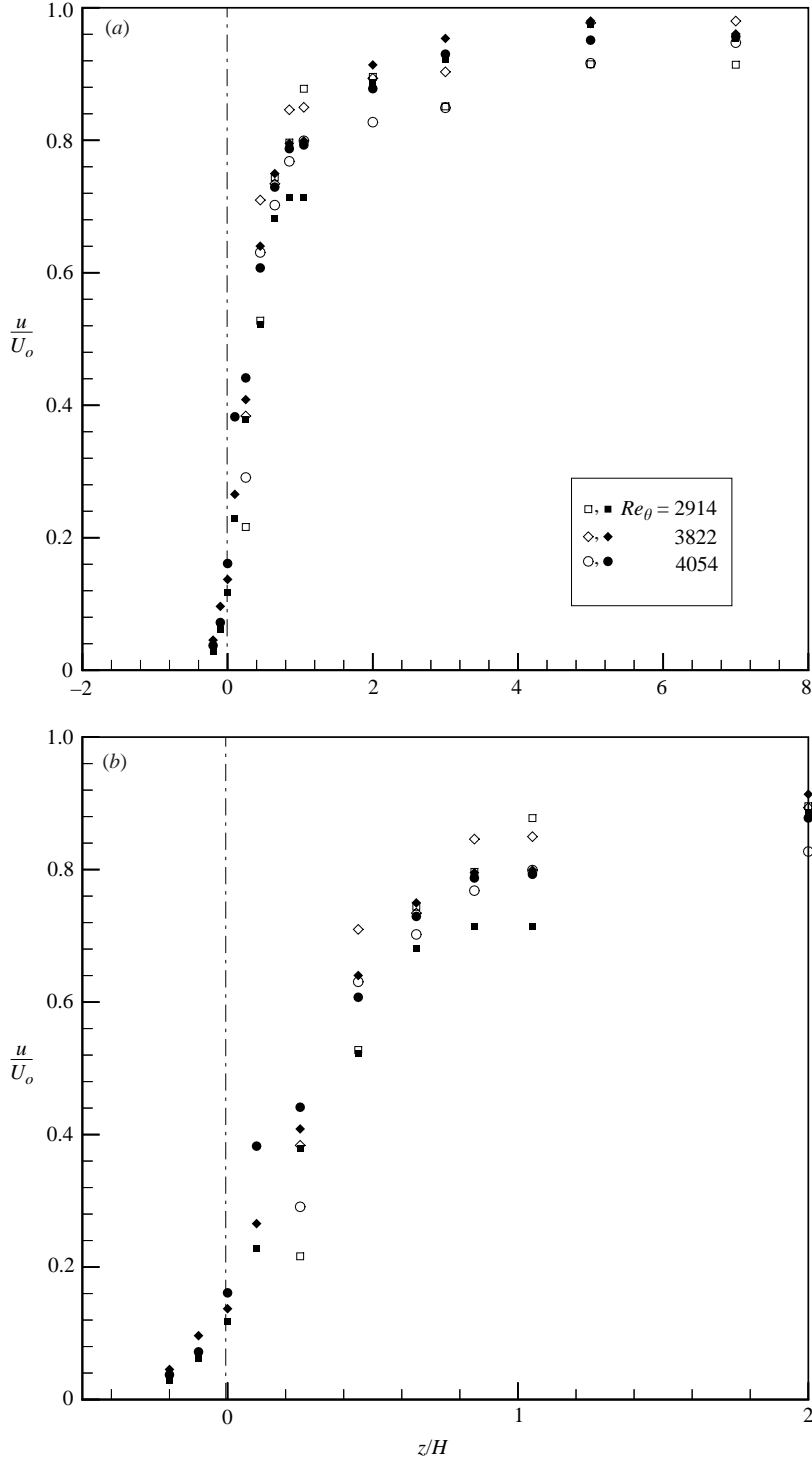
FIGURE 8. Normalized vertical profile of streamwise velocity at the mid-point of the cavity span: (*a*) The entire boundary layer, and (*b*) an expanded view of the boundary layer; cavity aspect ratio $A = 2$. Open symbols – without cavity; solid symbols – with cavity.

where

$$\Gamma(z^+) = 1 - e^{-z^+/B}, \tag{4.5}$$

R^* is the Reynolds number based on the friction velocity and channel height H, and $\Gamma(z^+)$ is the Van Driest damping function (White 1991, p. 438). The constants D_u, C and B are 2.3, 11.5 (based on the non-dimensional location of the peak r.m.s. velocity) and 0.32 (based on the slope at $z^+ = 0$). The normalized r.m.s. velocity distributions, both upstream and downstream of the cavity, indicate a fair agreement with (4.4).

In order to determine the effects of the cavity on its immediate surroundings, stream-wise velocity measurements taken along a vertical line passing through the centre of the cavity for cases with and without the cavity were compared. Figures 8(a, b) and 9 present normalized (with the free-stream velocity) vertical profiles of mean and r.m.s. streamwise velocity for these two cases at various Reynolds numbers Re_θ in the range 2914 to 4054 for $A = 2$. In the case where no cavity is present, the measurements extend only close to the channel floor (i.e. $z^+ \sim 5$). When the cavity is present, the non-dimensional position can become negative, given that $z = 0$ at the channel floor. It is evident from figure 8(a, b) that the presence of the cavity relieves the velocity gradient near the wall, but the peak r.m.s. velocity in the cavity increases by as much as 25% for $A = 2$ (figure 9). Since the production of turbulent kinetic energy is given by $-\overline{u'w'}\,\mathrm{d}u/\mathrm{d}z$, it appears that there is a substantial increase of Reynolds stresses to over-compensate for the reduction in the velocity shear so that there is an increase of turbulent kinetic energy production. As discussed, these extra Reynolds stresses can be generated by the inflow and outflow events associated with the cavity as envisioned by Djenidi *et al.* (1999). Outflow events ($w' > 0$) cause the low-momentum fluid to be transported to the overlying fluid (with $u' < 0$) and the opposite is also possible. Both of these momentum transport scenarios promote $-\overline{u'w'} > 0$.

5. Concentration field measurements

As described in §3, concentration measurements were performed downstream of the cavity using the LIF procedure. The LIF data were analysed, first, to extract scalar spectra at the cavity trailing edge in order to identify transport mechanisms from the cavity and, secondly, to quantify the distribution of cavity-filled contaminants downstream in the concentration boundary layer.

5.1. *Contaminant transport from the cavity*

As stated in §1, purging mechanisms in cavities have been studied before and the present work aims at studying the dispersion of purged material downstream. One of the important quantities in such studies is the fluctuation of concentration at the cavity trailing edge, just above the floor, which may act as an initial condition for downstream dispersion. figure 10(a, b) shows the spectra of scalar fluctuations measured at this location at $z^+ = zu_*/\nu = 6$–7, for the short ($A = 1$) and longer ($A = 2$) cavity width cases, where $Ri = \Delta b_o H/U^2 = 0.17$. A clear distinction can be seen between the two, which was also apparent in all other Ri cases. There are two identifiable spectral peaks which could be seen consistently for all $A = 2$ cases, in contrast to $A = 1$ cases wherein the spectral distribution is broad band without significant peaks. It also appears that the second peak frequency is a harmonic of the lower frequency.

The above observation can be attributed to the nature of the purging mechanism. Based on flow visualization, Armfield & Debler (1993) have identified removal
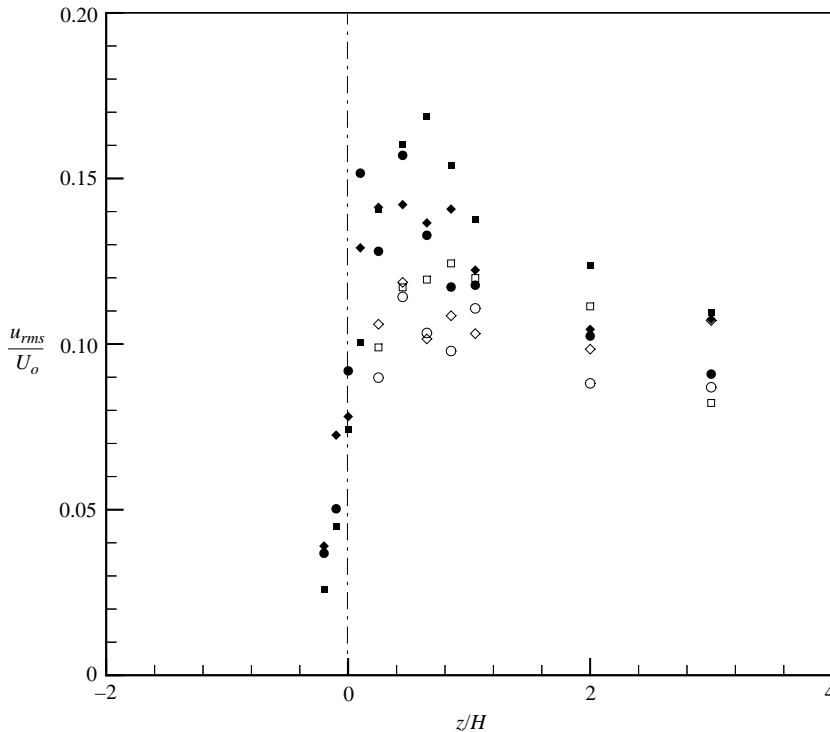
FIGURE 9. Normalized vertical profile of r.m.s. streamwise velocity at mid-point of cavity span; cavity aspect ratio $A = 2$. Symbols are the same as in figure 8.

mechanisms from cavities of different cavity aspect ratios. For $A \leqslant 1$, the removal occurs by transient seiching motions followed by continuous ejection of fluid from the cavity by the shear stresses exerted by the overlying skimming flow. Here circulatory motions are possible within the slot, but the transport of fluid out of the cavity is governed by the shear stresses (and buoyancy effects, or Ri); see the instantaneous concentration image in figure 11(*a*). This scenario is consistent with the continuous spectra observed in figure 10(*a*), where fluctuations corresponding to a continuous range of scales can be seen. For longer cavities ($A = 2$ case), however, the mechanism of purging is different, and is dominated by the separating vortices at the leading edge that mix up fluid at the interface (Armfield & Debler 1993), a phenomenon that is expected to be strongly dependent on Ri. It should be noted, however, that although in the presence of stratification such separated vortices have been observed only for longer cavities, in the absence of stratification the flow separation has been reported even for $A \sim 1$ (Townes & Sabersky 1966; Djenidi *et al.* 1999). Apparently, the buoyancy effects suppress the flow separation and subsequent mixing by the vortex–density interface interaction. The peaks of the spectra observed in figure 10(*b*) can be attributed to the periodic phenomena occurring in the flow separation, where cavity fluid ejections in the $A = 2$ case occur intermittently in a periodic fashion; see figure 11(*b*). The appearance of two dominant frequencies is a common occurrence in separated wake flows, the lower frequency corresponding to the shedding frequency and the higher frequency representing the separated shear layer instability frequency (e.g. Kim & Durbin 1988).
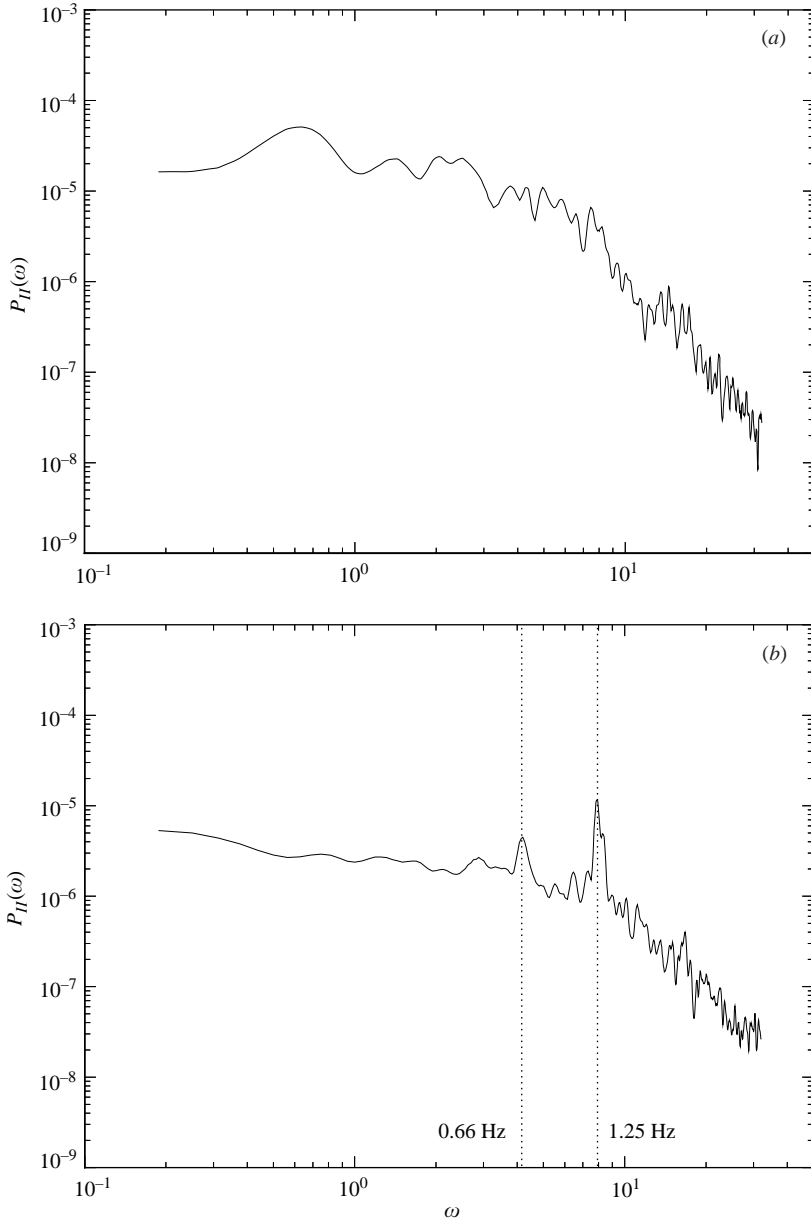
FIGURE 10. Concentration power spectrum taken at the trailing edge of the rectangular cavity for $Ri = 0.17$. (*a*) Cavity aspect ratio $A = 1$, and (*b*) $A = 2$. $Re_\theta = 2914$.

Figure 12 shows a plot of normalized buoyancy fluctuations at the same location $\sqrt{\overline{b'^2}}/\Delta b_o$ as a function of the Richardson number Ri for $A = 1$ and $A = 2$. For all Ri, the normalized buoyancy fluctuations immediately downstream of the cavity trailing edge are generally largest for the longer aspect ratio case $A = 2$, indicative of the effectiveness of the periodic cavity fluid ejection mechanism occurring at large aspect ratios.
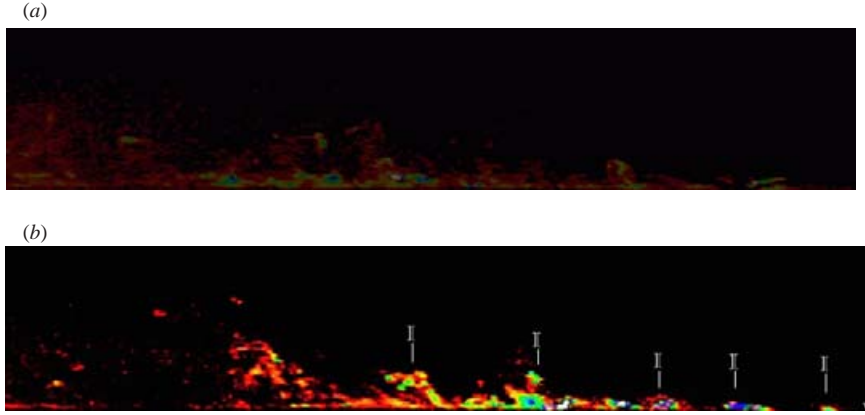
FIGURE 11. Instantaneous concentration image of cavity contaminant ejection and downstream dispersion for $Ri = 0.17$. (*a*) Cavity aspect ratio $A = 1$, and (*b*) $A = 2$. Note the intermittent ejection of the blobs, as indicated by I.
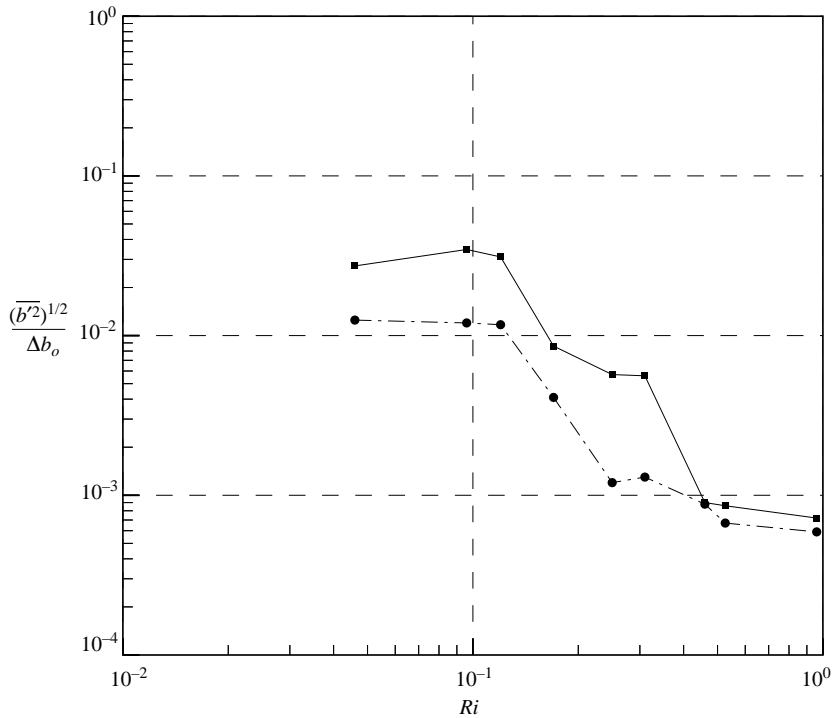

FIGURE 12. Normalized buoyancy fluctuations $(\overline{b'^2})^{1/2}/\Delta b_o$ at the cavity trailing edge as a function of Ri; $A = 1$ – solid circles, $A = 2$ – solid squares.

5.2. *Concentration distribution downstream of the cavity*

The concentration distribution downstream of the cavity, in general, is expected to be affected by three major processes, namely (i) the entrainment (entrance) of dense cavity fluid into the flow, (ii) the distortion of the incoming flow by the cavity,
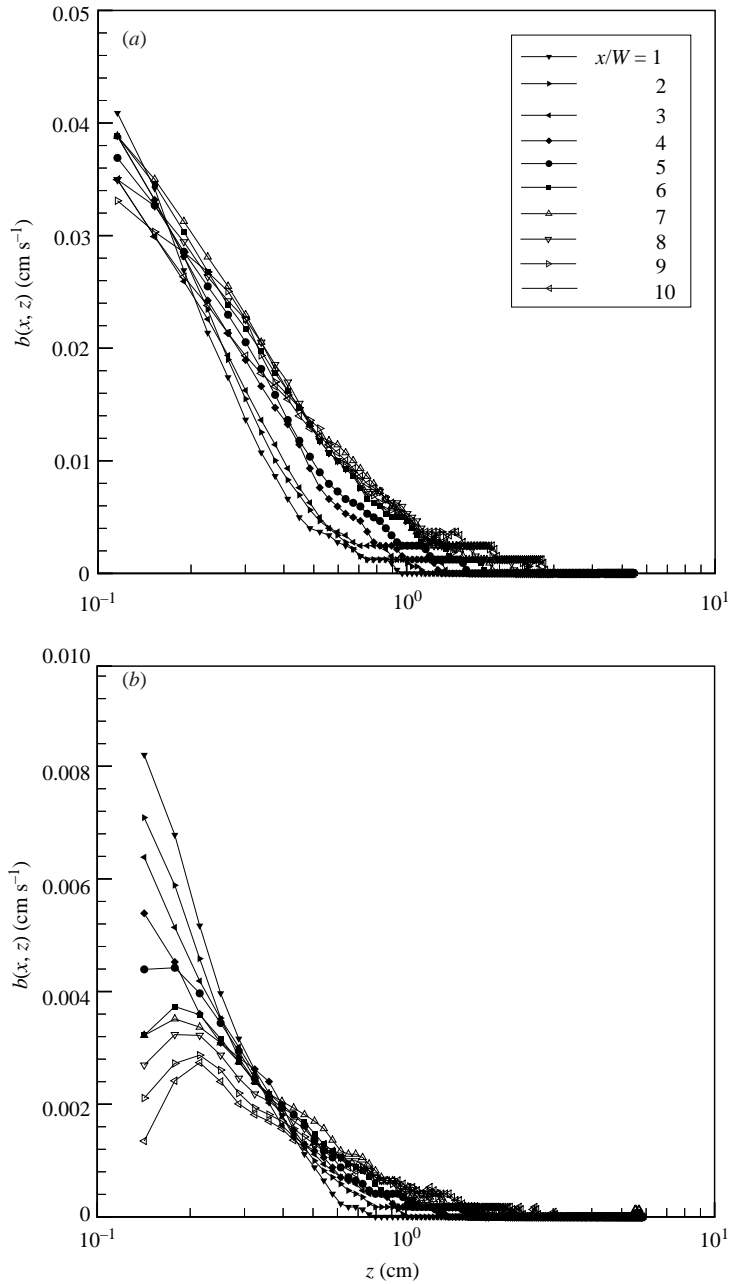
FIGURE 13(*a, b*). For caption see facing page.

and (iii) the distribution of entrained fluid within this downstream flow. Given that the distorted stream is expected to be relaxed to its upstream values at a certain downstream distance, the flow at short and intermediate distances from the cavity (which is considered herein) is a spatially non-equilibrium flow, but stationary in time. Observations show that once the dense fluid leaves the rectangular cavity, it is advected downstream while dispersing into the overlying fluid. Initially, wisps of fluid
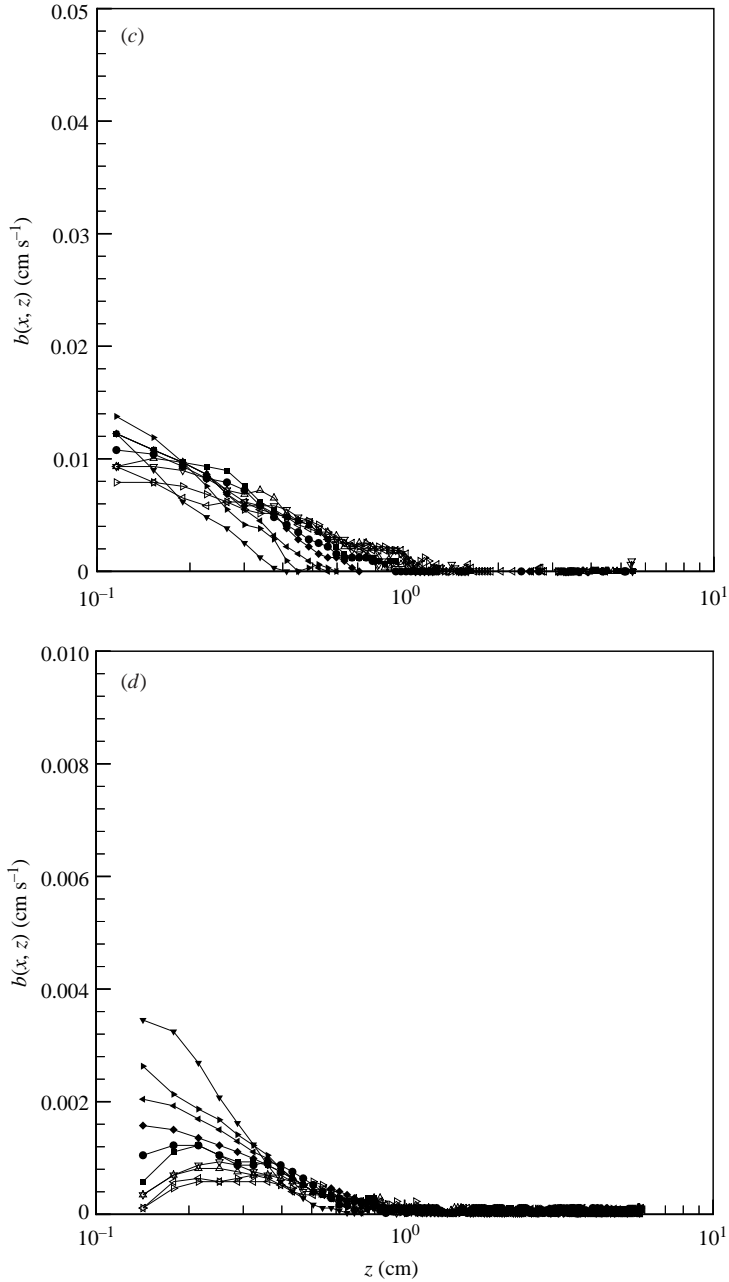
FIGURE 13. Vertical profiles of concentration boundary layer taken at multiple streamwise locations downstream from the cavity: (*a*) $Ri = 0.045$, (*b*) $Ri = 0.17$, (*c*) $Ri = 0.25$, and (*d*) $Ri = 0.96$; (*a, b*) $Re_\theta = 4054$, (*c, d*) $Re_\theta = 2914$; cavity aspect ratio $A = 2$.

ejected into the stream are distributed in the turbulent boundary layer, and these parcels of fluid are broken into smaller parcels (stirred) due to straining by turbulence and finally homogenized (mixed) with the background at molecular scales.

Figure 13(*a–d*) shows the measured mean concentration distribution at short and intermediate distances. The dimensional data do not collapse, clearly indicating the

importance of parameters such as the spatial location (x, z), cavity dimensions, and buoyancy effects. In order to develop a simple scaling relationship for how the downstream concentration is dependent on various governing parameters, the following simplified procedure was employed.

(i) The total flux (per unit width) of buoyancy crossing the horizontal plane at the top of the cavity (figure 1) can be written as

$$F = W(\overline{b'w'}) = WU_o\Delta b_o\left(\frac{\overline{b'w'}}{\Delta b_o U_o}\right), \tag{5.1}$$

where Δb_o is the buoyancy jump across the interface, U_o is the free-stream velocity, and w' and b' are the instantaneous vertical velocity and buoyancy fluctuations, respectively. Note that $\overline{b'w'}/\Delta b_o U_o$ takes the form of an entrainment coefficient $E = u_e/U_o$, where u_e is the entrainment velocity at the density interface (see Strang & Fernando 2001). Parameterizing E based on (2.3), i.e.

$$E = f_1(Ri, A), \tag{5.2}$$

where f_1, f_2, ... are functions, it is possible to write

$$F = WU_o\Delta b_o f_1(Ri, A). \tag{5.3}$$

(ii) The material entering the stream via entrainment dilutes sufficiently rapidly that it does not have an effect on the flow above (Strang & Fernando 2001). However, the flow is distorted by the cavity itself, in much the same way as described in §4 for the unstratified case, but to a lesser extent due to the shielding of flow from the cavity by the strong density interface. The distorted flow relaxes back to the upstream conditions gradually. The shape of the velocity profiles during the adjustment process changes only slowly. For example, as evident from figure 5(a, b), the normalized mean profiles appear to have a logarithmic region in $0 < x/W < 7$ and its variation is less than $\pm 9\%$ for a given A. However, the magnitude of the normalized velocity profiles are sensitive to A. Assuming self-similar profiles in the short and intermediate range, the general mean velocity profile at any x can be written in terms of the local friction velocity as

$$\frac{u}{u_*} = f_2\left(\frac{z}{\delta_m}\right), \tag{5.4}$$

where u_* is the local friction velocity, and δ_m is the momentum boundary layer thickness, both of which are dependent on A. The local friction velocity can be represented as $u_* = U_o f_3(A)$, assuming slow variation of u_* over short and intermediate distances $(x/W < 7)$. Thus, (5.4) becomes

$$u = U_o f_4\left(\frac{z}{\delta_m}, A\right). \tag{5.5}$$

(iii) Assuming that the processes are in local equilibrium, the mean concentration boundary layer profiles can be represented in the form of self-similar profiles based on local variables,

$$b = b^* f_5\left(\frac{z}{\delta_b}\right), \tag{5.6}$$

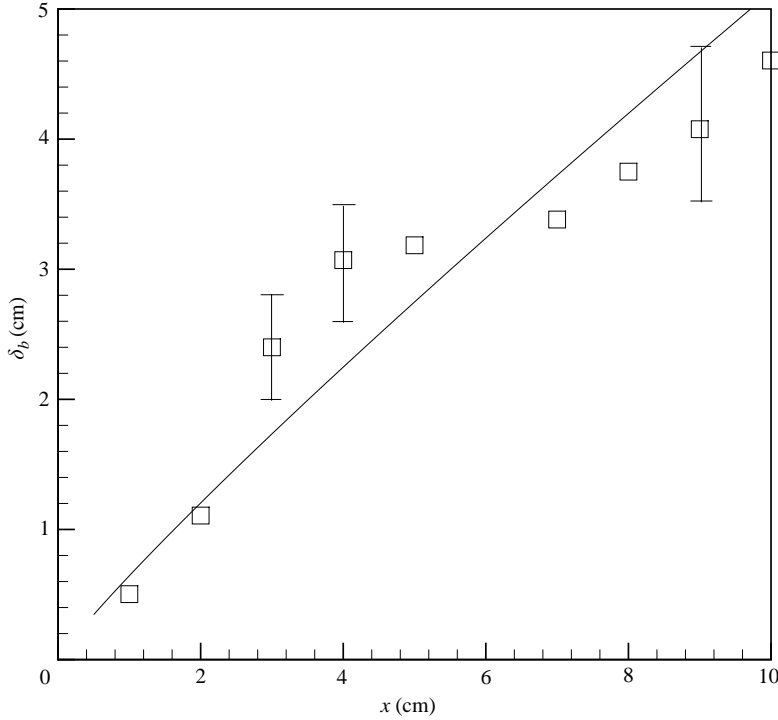where δ_b is the concentration boundary layer thickness, and b^* is a local concentration scale.

FIGURE 14. Average dimensional buoyancy layer thickness δ_b versus the dimensional streamwise distance x for $A = 2$. For $x > 1\,\mathrm{cm}$, $\delta_b \propto x^{0.91}$ (as indicated by the solid line).

(iv) The streamwise advection of buoyancy by the mean flow is expected to dominate the turbulent flux, i.e. $bu > \overline{b'u'}$, and thus

$$F \simeq \int_0^{\delta_b} bu \, \mathrm{d}z. \tag{5.7}$$

Using (5.5), (5.6) and (5.7), we obtain

$$F \simeq \delta_b b^*(x) U_o \int_0^1 f_4\left(\xi \frac{\delta_b}{\delta_m}, A\right) f_5(\xi) \, \mathrm{d}\xi, \tag{5.8}$$

where $\xi = z/\delta_b$.

Since the boundary layer of the flow approaching the cavity is fully developed, even though it is perturbed over the cavity, the velocity profile (and hence, $f_4(\xi\delta_b/\delta_m, A)$) near the channel bottom, downstream of the cavity, was steep up to about $0.5\,\mathrm{cm}$ followed by a slowly varying trend. On the other hand, the concentration within the boundary layer and, hence, f_5 monotonically decreases with increasing ξ. Overall, for a given value of A, the integral expressed in (5.8) can be taken as approximately constant within $\pm 10\%$ and, hence using (5.3)

$$W U_o \Delta b_o f_1(Ri, A) \propto \delta_b b^* U_o f_6(A), \tag{5.9}$$

where $f_6(A)$ represents the cumulative A dependence in the integral of (5.8). The concentration boundary layer thickness δ_b downstream of the cavity can be estimated
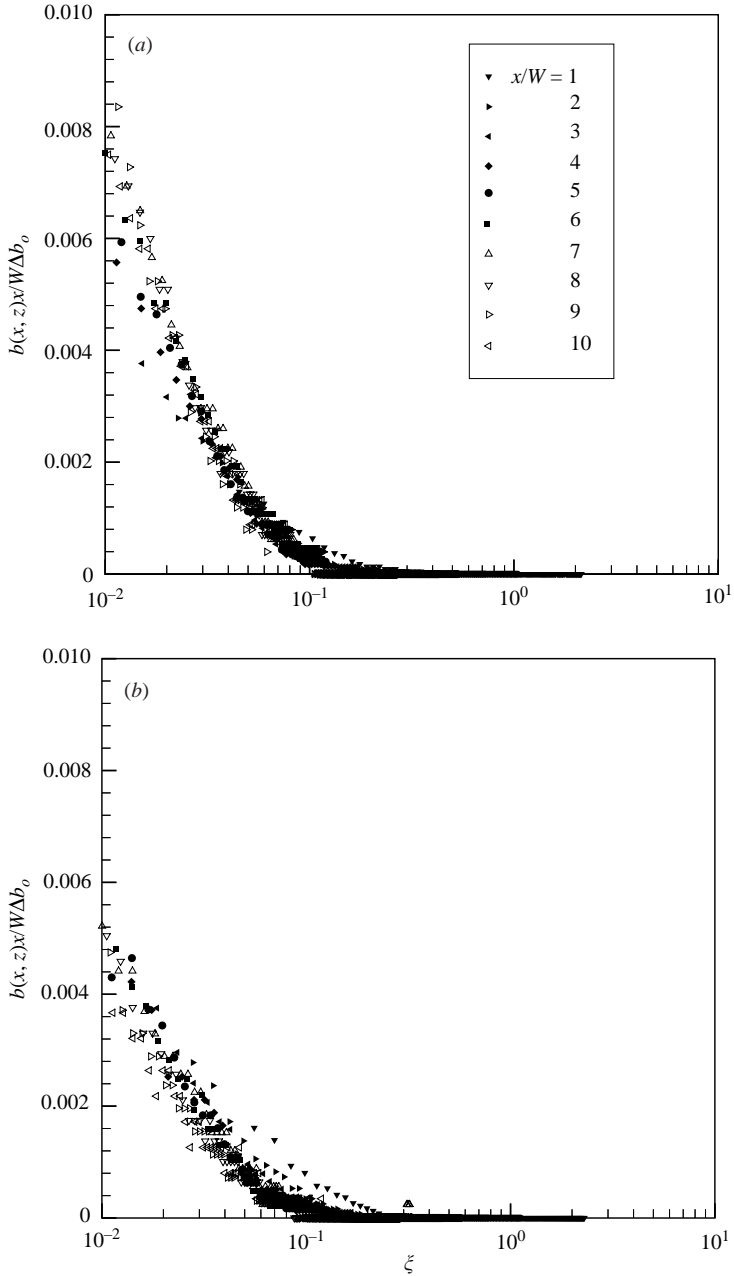
FIGURE 15(*a*, *b*). For caption see facing page.

by considering the vertical dispersion of the contaminants in the boundary layer as

$$\frac{\mathrm{d}\delta_b^2}{\mathrm{d}t} \sim U_o \frac{\mathrm{d}\delta_b^2}{\mathrm{d}x} \sim K_e, \tag{5.10}$$

where K_e is the eddy diffusivity. By using the parameterization $K_e \sim u^* z \sim u^* \delta_b$ (which neglects buoyancy effects on dispersion) for the edge of the concentration boundary
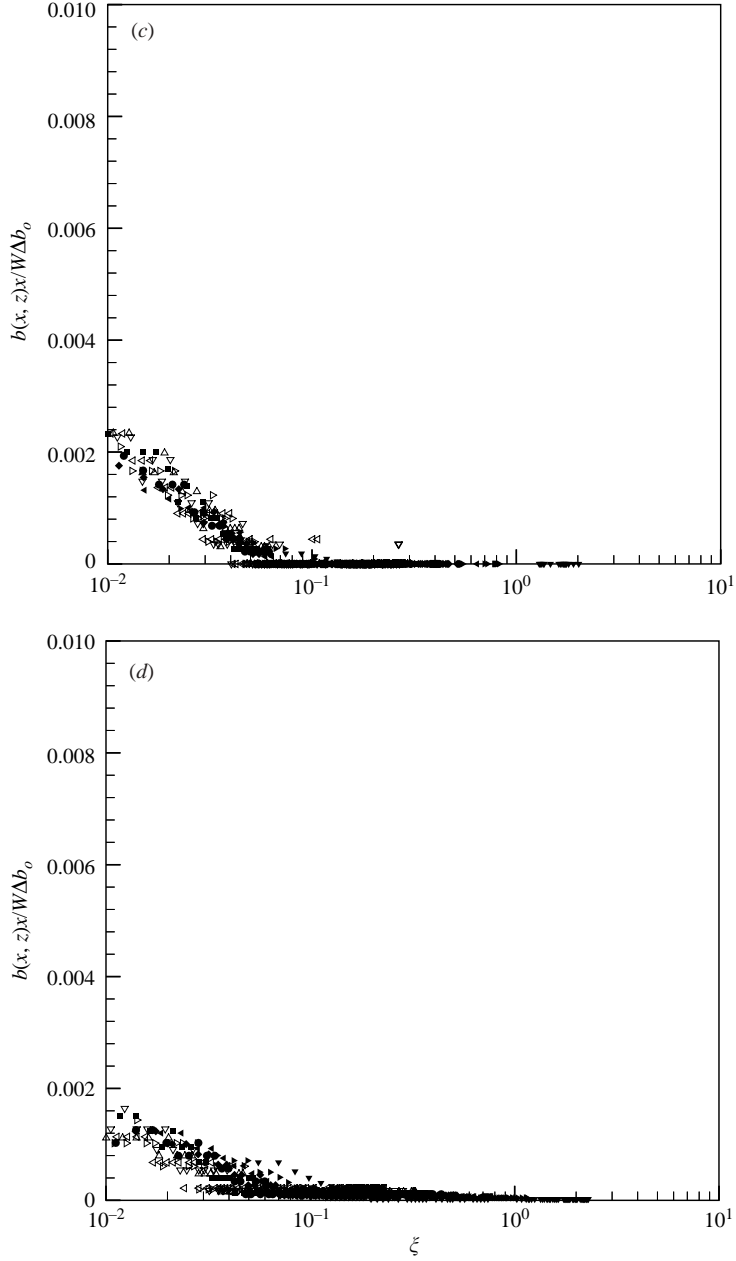
FIGURE 15. Vertical profile of concentration boundary layer taken at multiple streamwise locations downstream from the cavity: (a) $Ri = 0.046$, (b) $Ri = 0.17$, (c) $Ri = 0.25$, and (d) $Ri = 0.96$; data normalized using scaling in (5.12); (a, b) $Re_\theta = 4054$, (c, d) $Re_\theta = 2914$; cavity aspect ratio $A = 2$.

layer, (5.10) yields

$$\delta_b \sim x f_3(A). \tag{5.11}$$

The concentration boundary layer thickness δ_b was determined at a distance from the wall where the averaged buoyancy fell to less than 1% of the peak averaged buoyancy
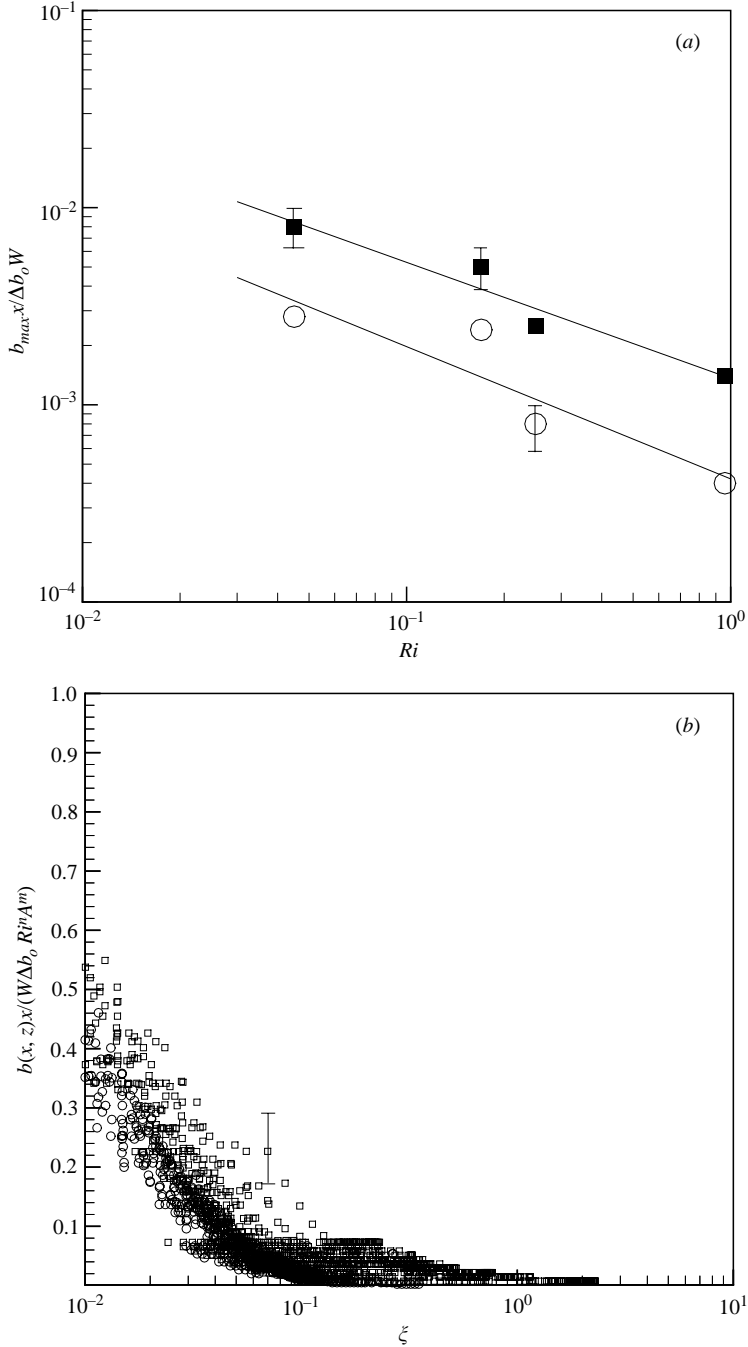
FIGURE 16. Plot of the maximum (scaled) boundary layer concentration $b_{max}x/\Delta b_o W$ (*a*) as a function of the Richardson number Ri and cavity aspect ratio A; and (*b*) collapsed data for both Ri and A (circles: $A = 1$; squares: $A = 2$).

in the boundary layer. Although only a single realization is shown in figures 11(*a*) and 11(*b*), some support for this linear growth was evident visually. Quantitative measurements, shown in figure 14, also show that (5.11) is approximately satisfied

with $\delta_b \propto x^{0.91}$ for $A = 2$, and a similar power law was observed for $A = 1$. Although the contaminants emanating from the cavity have a certain amount of buoyancy, the turbulence therein is strong enough to disperse the contaminat fluid parcels in the boundary layer as if the buoyancy forces were negligible. The buoyancy influence is further reduced as the distance from the cavity increases. Using (5.9) and (5.11), the concentration scaling can be proposed as

$$b^* \sim \frac{W \Delta b_o}{x} G(Ri, A), \tag{5.12}$$

where $G(Ri, A)$ is a function taking into account f_3 and f_6. Thus, (5.6) becomes

$$b(x, z) = \frac{W \Delta b_o}{x} G(Ri, A) f_5(\xi). \tag{5.13}$$

For a given experiment, $G(Ri, A)$ is fixed and hence b is expected to vary with $W \Delta b_o / x$ and ξ.

Figure 15(*a–d*) presents the same data as figure 13(*a–d*) but normalized using the scaling based on (5.13), i.e. $W \Delta b_o / x$. A good collapse can be noted for each Ri. For some concentration measurements, rather larger scatter can be seen at small x/W values and large Ri, perhaps because of the prolonged retention of the buoyancy influence of contaminant particles even after they leave the cavity (which was assumed to be negligible in the analysis).

Note that $W \Delta b_o / x$ does not represent the full buoyancy scaling, and the function $G(Ri, A)$ should be included if the scaling is to be generally applicable. If one assumes that $G \simeq C(Ri^n A^m)$, where C is a constant, then n can be evaluated by inspecting the collapsed concentration data, for example the dependence of the maximum normalized concentrations $b_{max}/(W \Delta b_o / x)$ on Ri. Such a log–log plot is shown in figure 16(*a*), based on the average value of the maximum normalized concentration in figure 15(*a–d*) and similar plots based on $A = 1$. The two slopes are -0.68 ± 0.15 and -0.59 ± 0.15, respectively, and an average value of $n = -0.64$ can be proposed.

Finally, it would have been useful if m had been evaluated using experiments carried out with a range of A values. However, during our experimental programme only two values of A were used, and hence only a rough estimate of m and C could be made as $m = 1.73$. Figure 16(*b*) shows a plot of $b(x, z)/[(W \Delta b_o / x) Ri^n A^m]$ as a function of ξ. The collapse is reasonable and, hence, it appears to be consistent with the above power-law form. However, it is hoped that future experiments will document n and m based on a more extensive set of measurements.

6. Summary

The concentration distribution, at short and intermediate distances downstream, resulting from the purging (flushing) of dense soluble contaminants from a two-dimensional rectangular cavity by an overlying turbulent shear flow was investigated using a laboratory experiment. Turbulent mixing at the interface between the dense pool and flow above causes contaminant to be entrained and transported downstream. Of major interest was the parameterization of downstream concentration at short and moderate distances from the source, with the aim of applying the results to practical situations such as accidental dense chemical spills or deliberate releases in complex topographies. The relaxation of turbulence downstream of the cavity was also of

interest, as it is an important quantity in modelling flow downstream of urban roughness canopies.

Two aspect ratios were used, $A = 1$ and 2. The measurement of the velocity field surrounding the cavity, especially downstream of the trailing edge, showed that a cavity with $A = 1$ has only a small effect on the friction velocity. This observation is consistent with that of Pearson, Elavarasan & Antonia (1997), except that they reported oscillations of the skin friction coefficient. In particular, they noted an increase in the skin friction coefficient immediately downstream of the trailing edge, with recovery to the nominal value within one boundary layer thickness downstream (~ 3 cm in their experiments). Thereafter, the skin friction coefficient weakly oscillated about the nominal (upstream) value until the oscillations were damped approximately ten boundary layer thicknesses downstream. Perhaps, the difference in results can be attributed to the low values of Reynolds numbers used in their experiments, i.e. $Re_\theta \sim 700$.

Conversely, the downstream boundary layer responded to the larger aspect ratio cavity ($A = 2$) with a moderate ($\sim 20\%$) increase in the friction velocity immediately downstream of the trailing edge and a slow recovery to the nominal value. Over the downstream measurement distance of $x = 7W$, the boundary layer did not completely relax to the far upstream values, but the relaxation process itself was clearly evident. The velocity field statistics above the cavity location, both with and without the cavity, indicated a local relief in the mean velocity gradient in the streamwise velocity when the cavity is present. The turbulent intensity for the $A = 2$ case, however, was stronger in the presence of the cavity. Increased Reynolds stresses associated with strong intermittent entrainment (inflow and outflow) events at the brim of the cavity explain this observation.

Previous flow visualization studies (Debler & Armfield 1993) have shown that for $A \sim 1$ the entrainment occurs by continuous ejection of wisps of fluid out of the cavity whereas $A > 1$ is characterized by the periodic release of cavity fluid by separated flow at the cavity leading edge. Spectral measurements in the present study confirmed these observations. Laser-induced fluorescence measurements of concentration, and hence the buoyancy profiles taken at various intermediate downstream distances, can be collapsed using the scaling variable $b^* = (W \Delta b_o / x) G(Ri, A)$ for the buoyancy. The function G was evaluated experimentally and found to be consistent with the form $G \propto Ri^n A^m$, with $n \simeq -0.64$ and $m \simeq 1.73$. Since only two values of A were used, further studies are necessary to investigate the dependence of G on A over a wide parameter range.

REFERENCES

ARMFIELD, S. W. & DEBLER, W. 1993 Purging of density stabilized basins. *J. Heat Mass Transfer* **36**, 519–530.

BERNARD, P. S. & WALLACE, J. M. 2002 *Turbulent Flow: Analysis, Measurement, and Prediction.* Wiley.

BRIGGS, G. A., THOMPSON, R. S. & SNYDER, W. H. 1990 Dense gas removal from a valley by crosswinds. *J. Hazardous Mater.* **24**, 1–38.

CASTRO, I. P., KUMAR, A., SNYDER, W. H. & ARYA, S. P. S. 1993 Removal of slightly heavy gases from a valley by crosswinds. *J. Hazardous Mater.* **34**, 271–293.

DEBLER, W. & ARMFIELD, S. W. 1997 The purging of saline water from rectangular and trapezoidal cavities by an overflow of turbulent sweet water. *J. Hydraul. Res.* **1**, 43–62.

DEBLER, W. & IMBERGER, J. 1996 Flushing criteria in estuarine and laboratory experiments. *J. Hydraul. Engng* 728–734.

DESILVA, I. P. D., MONTENEGRO, L. & FERNANDO, H. J. S. 1990 Measurement of interfacial distortions at a stratified entrainment interface. *Exps. Fluids* **9**, 174–177.

DJENIDI, L., ELAVARASAN, R. & ANTONIA, R. A. 1999 The turbulent boundary layer over transverse square cavities. *J. Fluid Mech.* **395**, 271–294.

FERNANDO, H. J. S. 1991 Turbulent mixing in stratified fluids. *Annu. Rev. Fluid Mech.* **23**, 455–493.

FERNANDO, H. J. S. & HUNT, J. C. R. 1996 Some aspects of turbulence and mixing in stably stratified layers. *Dyn. Atmos. Oceans* **23**, 35–62.

KIM, H. J. & DURBIN, P. A. 1988 Observation of the frequencies in a sphere wake and of drag increase by acoustic excitation. *Phys. Fluids* **31**, 3260–3265.

NEZU, I. & NAKAGAWA, H. 1993 *Turbulence in Open Channel Flows*. IAHR.

ODELL, G. M. & KOVASZNAY, L. S. G. 1971 A new type of water channel with density stratification. *J. Fluid Mech.* **50**, 535–543.

PEARSON, B. R., ELAVARASAN, R. & ANTONIA, R. A. 1997 The response of a turbulent boundary layer to a square groove. *Trans. ASME: J. Hydraul. Engng* **119**, 466–469.

SCHLICHTING, H. 1987 *Boundary-layer Theory*, 2nd Edn. Reissue. McGraw Hill.

SEETO, C. M. 1987 An experimental study of entrainment at a density interface by mean velocity shear. Thesis, Dept. Mech. Engng University of Canterbury (New Zealand), 230 pp.

STRANG, E. J. & FERNANDO, H. J. S. 2001 Entrainment and mixing in a stratified shear flows. *J. Fluid Mech.* **428**, 349–386.

TENNEKES, H. & LUMLEY, J. L. 1972 *A First Course in Turbulence*. The MIT Press.

TOWNES, H. W. & SABERSKY, R. H. 1966 Experiments on the flow over a rough surface. *Intl J. Heat Mass Transfer* **9**, 729–738.

WHITE, F. M. 1991 *Viscous Fluid Flow*. McGraw-Hill.